

# Edge Transport Barrier Models for Simulating H-Mode Operation Scenarios in DEMO with Integrated Plasma Transport Code TOTAL

Yoshihiro ITAKURA, Takaaki FUJITA and Atsushi OKAMOTO

*Graduate School of Engineering, Nagoya University, Furo-cho, Chikusa-ku, Nagoya 464-8603, Japan*

(Received 20 March 2021 / Accepted 16 February 2022)

Edge transport barrier (ETB) models are developed and introduced into an integrated transport code TOTAL. The transitions between L-mode and H-mode are triggered by comparing the net heating power with the threshold powers. At the L to H transition, quick reduction in transport in the pedestal region causes back transition due to reduced net heating power and then gradual change in the transport in the pedestal region is needed. The pedestal pressure is adjusted to the value predicted by an empirical scaling. Three models, the PID control model, the ELM model, and the empirical continuous ELM model, are compared for the pedestal pressure control. The control is possible in all of three models but it is observed that larger pellet injection is needed to increase the density and a lower pedestal density is obtained in the ELM model. During tungsten injection, the pedestal pressure is well controlled in the empirical continuous ELM model and in the PID control model.

© 2022 The Japan Society of Plasma Science and Nuclear Fusion Research

Keywords: pedestal, H-mode transition, ELM, threshold power, impurity transport

DOI: 10.1585/pfr.17.1403016

## 1. Introduction

In ITER and DEMO, in order to obtain confinement performance for fusion power generation, it is necessary to maintain H-mode plasma in which a transport barrier is formed at the plasma boundary. Impurity injection is planned in DEMO to reduce the heat load on the divertor target. There is concern about confinement deterioration and back transition to L mode due to increased radiation power by impurity accumulation in the core, and then simulations that take them into consideration are required. For instance, time-dependent behavior of H-mode operation in ITER was studied in Ref. [1], which included maintaining H mode against increased H-mode threshold power caused by density rise after H-mode transition and back transition due to radiation caused by tungsten. In an integrated transport code TOTAL, the H-mode plasma was conventionally simulated by multiplying the thermal/particle diffusivity by factors less than unity. The values of the factors were given in an input file and were fixed during the simulation [2]. The values were determined so as to achieve the confinement enhancement factor (H factor) of the design value in typical plasma conditions. Two issues were recognized in this treatment. The first one is that the H-mode is maintained through the whole period of the simulation and then it is not possible to simulate L to H transition and H to L transition, which take place either intentionally or unintentionally. The second one is that the plasma pressure at the pedestal top depends on the heat flux through the pedestal,

while it is in fact determined by the stability limit or edge localized modes (ELMs). We have developed new edge transport models in TOTAL to resolve these issues in order to perform realistic simulation of H-mode operation. Simulation of transition to H-mode from L-mode and vice versa has become possible by monitoring the net heating power and threshold power for transition during the simulation. Control of the pedestal pressure has become possible by adjusting or changing transiently the thermal diffusivity at the pedestal region. The rest of this paper is organized as follows. In Sec. 2, the newly developed H-mode transition model and the pedestal pressure control models are described, together with the heat and particle transport models used in TOTAL. Section 3 describes plasma parameters and conditions used in this work. Results of simulations with three models for pedestal pressure control are presented in Sec. 4. An example of simulation on impurity injection into H-mode plasma is shown in Sec. 5. Finally summary is given in Sec. 6.

## 2. Models

### 2.1 Heat and particle transport model

The transport of heat and particles in the plasma is divided into neoclassical transport and anomalous transport. In this study, the following mixed Bohm / Gyro-Bohm model is used as the anomalous heat transport model [3]. In this model, the anomalous thermal diffusivities for electrons and ions,  $\chi_e^{\text{AN}}$  and  $\chi_i^{\text{AN}}$  consist of Bohm terms  $\chi_{\text{Be}}$ ,

author's e-mail: fujita@energy.nagoya-u.ac.jp

$\chi_{\text{Bi}}$  [4] and Gyro-Bohm terms  $\chi_{\text{gBe}}$ ,  $\chi_{\text{gBi}}$  [5]:

$$\chi_e^{\text{AN}} = \chi_{\text{Be}} + \chi_{\text{gBe}}, \quad (1)$$

$$\chi_i^{\text{AN}} = \chi_{\text{Bi}} + \chi_{\text{gBi}}, \quad (2)$$

$$\chi_{\text{Bi}} = 2\chi_{\text{Be}}, \quad (3)$$

$$\chi_{\text{gBi}} = \chi_{\text{gBe}}. \quad (4)$$

The  $\chi_{\text{Be}}$  and  $\chi_{\text{gBe}}$  are determined by the formulas shown below, which include the scale length of the electron pressure  $L_p$  and that of the electron temperature:

$$\chi_{\text{Be}} = \alpha_B \frac{aT_e}{B_t} L_p^{-1} q^2 \times \frac{T_e(0.8\rho_{\text{pedtop}}) - T_e(\rho_{\text{pedtop}})}{T_e(\rho_{\text{pedtop}})}, \quad (5)$$

$$L_p^{-1} = \frac{|\nabla p_e|}{p_e}, \quad (6)$$

$$\chi_{\text{gBe}} = \alpha_{\text{gB}} \frac{a|\nabla T_e|}{B_t} \rho^*, \quad (7)$$

$$\rho^* = \frac{1}{aZ_i B_t} \sqrt{\frac{MT_e}{e}}, \quad (8)$$

where  $a$  is the plasma minor radius in m,  $T_e$  is the electron temperature in eV,  $B_t$  is the toroidal field in T,  $p_e$  is the electron pressure,  $q$  is the safety factor. By comparison with the H-mode plasma experiment, the values of coefficients  $\alpha_B$  and  $\alpha_{\text{gB}}$  are given as  $\alpha_B = 8.0 \times 10^{-5}$  and  $\alpha_{\text{gB}} = 3.5 \times 10^{-2}$  [5].

In particle transport, fluxes of  $\text{D}^+$ ,  $\text{T}^+$  and  $\text{He}^{2+}$  are calculated and the flux of electrons is determined by charge neutrality. The anomalous particle diffusivity is determined by  $\chi_e^{\text{AN}}$  and  $\chi_i^{\text{AN}}$  as follows.

$$D^{\text{AN}} = (0.3 + 0.7(1 - \rho)) \frac{\chi_e^{\text{AN}} \chi_i^{\text{AN}}}{\chi_e^{\text{AN}} + \chi_i^{\text{AN}}}, \quad (9)$$

The pinch velocity by anomalous transport  $V^{\text{AN}}$  is assumed and is given by

$$V^{\text{AN}} = -C_p D^{\text{AN}} (2r/a^2), \quad (10)$$

where  $C_p$  is a dimensionless coefficient for varying the anomalous pinch velocity and then the electron density profile. In this study its value is fixed as  $C_p = 0.5$ .

In simulation with impurity injection described in Sec. 5, the impurity ion density is determined by solving the rate equation with transport terms. The detail is given in Ref. [6]. The neoclassical flux of impurity is calculated with the NCLASS module [7]. The anomalous diffusivity of impurity ions is assumed to be twice as that of the neoclassical diffusivity. Anomalous pinch of impurity ions is given by the same formula as Eq. (10).

## 2.2 H-mode transition model

An algorithm has been introduced to trigger the transition from L-mode to H-mode and that from H-mode to

L-mode, comparing the net heating power and the H-mode threshold power. The net heating power  $P_{\text{net}}$  is equivalent to the power crossing the plasma edge or the separatrix and is calculated by

$$P_{\text{net}} = P_\alpha + P_{\text{ohm}} + P_{\text{RF}} - P_{\text{rad}} - \frac{dW}{dt}, \quad (11)$$

where  $P_\alpha$  is the alpha heating power,  $P_{\text{ohm}}$  is the ohmic heating power,  $P_{\text{RF}}$  is the external heating power supplied by RF,  $P_{\text{rad}}$  is the radiation power and  $dW/dt$  is the time-derivative of the plasma thermal energy. As the H-mode threshold power  $P_{\text{LH}}$ , the formula given in Ref. [8] multiplied by 0.8 is used:

$$P_{\text{LH}} = 0.8 \times 0.0488 \bar{n}_{20}^{0.717} B_t^{0.803} S^{0.941},$$

where  $\bar{n}_{20}$  is line average density in  $10^{20} \text{m}^{-3}$  and  $S$  is the plasma surface area in  $\text{m}^2$ . The factor 0.8 is included to consider that  $P_{\text{LH}}$  is inversely proportional to the ion mass number  $M$  and that DT plasma with  $M = 2.5$  is used in this work while D plasma with  $M = 2$  is assumed in the formula given in Ref. [8].

The  $P_{\text{net}}$  and  $P_{\text{LH}}$  are calculated at every time step during the simulation. When  $P_{\text{net}} > P_{\text{LH}}$  is satisfied in L-mode, transition to H-mode is triggered, while when  $P_{\text{net}} < P_{\text{HL}} = 0.5P_{\text{LH}}$  is satisfied in H-mode, back transition to L-mode is triggered. The lower value of  $P_{\text{HL}}$  than  $P_{\text{LH}}$  is assumed based on the experimental results observed in ASDEX Upgrade that high confinement was maintained even with  $P_{\text{net}} < P_{\text{LH}}$  [9]. The heat diffusivities  $\chi_e^{\text{AN}}$  and  $\chi_i^{\text{AN}}$  are multiplied by factors  $C_e$  and  $C_i$ , called enhancement factors, to simulate the transport barrier (pedestal) in  $0.95 < \rho < 1$ , where  $\rho$  is the normalized minor radius, as shown in Fig. 1:

$$\chi_{e \text{ ped}}^{\text{AN}} = C_e \chi_e^{\text{AN}}, \quad (12a)$$

$$\chi_{i \text{ ped}}^{\text{AN}} = C_i \chi_i^{\text{AN}}. \quad (12b)$$

In H-mode,  $C_e$  and  $C_i$  are set less than unity:  $C_e = C_{e0} = 0.007$ ,  $C_i = C_{i0} = 0.0035$ , while in L-mode they are set to unity. Note that the values of  $C_e$  and  $C_i$  are changed in

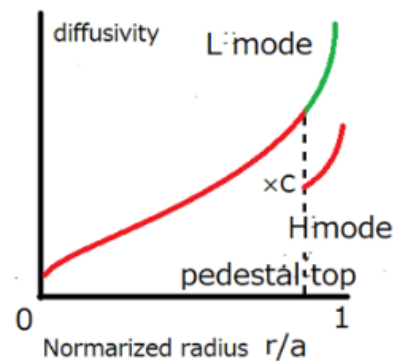


Fig. 1 Schematic view of radial profile of diffusivity in H-mode (red) and in L-mode (green).

the control of the pedestal pressure as described in Sec. 2.3. The ratio between  $C_{e0}$  and  $C_{i0}$  was determined so that similar pedestal temperatures would be obtained for electrons and ions. The values of  $C_{e0}$  and  $C_{i0}$  were determined so that the pedestal pressure would reach, but not exceed too much, the value predicted by scaling law at the start of control of pedestal pressure.

At the transition,  $C_e$  and  $C_i$  are not changed immediately but are changed gradually over 5 s as shown in Fig. 2. If  $C_e$  and  $C_i$  are reduced like step function at the H-mode transition, large positive  $dW/dt$  is generated which reduces  $P_{\text{net}}$  below  $0.5P_{\text{LH}}$  and the back transition is triggered. Large negative  $dW/dt$  is then generated just after the back transition, which increases  $P_{\text{net}}$  above  $P_{\text{LH}}$  and then the H-mode transition is triggered. This process is repeated for several seconds. Gradual change in  $C_e$  and  $C_i$  is introduced to avoid this oscillation phenomena. In Fig. 2, the L to H transition is triggered at  $t = 10.6$  s when  $P_{\text{net}}$  exceeds  $P_{\text{LH}}$ .  $C_e$  and  $C_i$  are changed during the transition phase between  $t = 10.6$  and 15.6 s according to the formula shown below

$$C_e = C_{e0} + (1 - C_{e0}) \left( \frac{t_1 + \tau_{\text{tr}} - t}{\tau_{\text{tr}}} \right)^5, \quad (13a)$$

$$C_i = C_{i0} + (1 - C_{i0}) \left( \frac{t_1 + \tau_{\text{tr}} - t}{\tau_{\text{tr}}} \right)^5, \quad (13b)$$

where  $t_1$  is the time that the transition was triggered and  $\tau_{\text{tr}}$  is the duration of transition, 5 s. The  $P_{\text{net}}$  continues to decrease during the transition phase even with the gradual change in  $C_e$  and  $C_i$ . Heating power during this phase, 120 MW, was determined to sustain  $P_{\text{net}}$  above  $P_{\text{HL}}$ . The  $P_{\text{net}}$  starts to rise again at  $t = 14.3$  s due to increase in alpha heating power. In this example, PID control of the pedestal pressure by  $C_e$  and  $C_i$  is done after the end of transition phase, though the change in  $C_e$  and  $C_i$  are small

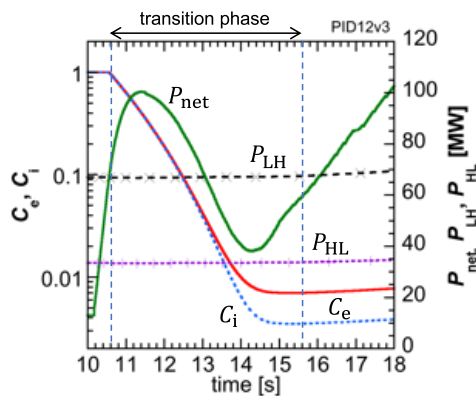


Fig. 2 Time evolution of the enhancement factors  $C_e$  (red solid line) and  $C_i$  (blue dotted line), net heating power  $P_{\text{net}}$  (green solid line), L to H transition power (black dashed line) and H to L transition power  $P_{\text{HL}}$  (magenta dotted line). High external heating power of 120 MW was applied during  $t = 10$  s to 15 s.

in the period shown in the figure.

### 2.3 Pedestal pressure control model

It is intended to keep the pedestal pressure to the value predicted by a scaling law obtained by experiment data. The scaling law of pressure at the pedestal top  $p_{\text{ped}}^{\text{scl}}$  given in Ref. [10] is used in this work:

$$p_{\text{ped}}^{\text{scl}} = \frac{2}{3} \times \frac{W_{\text{ped}}^{\text{scl}} \times 10^6}{0.92V_p}, \quad (14)$$

$$W_{\text{ped}}^{\text{scl}} = 0.000643 I_p^{1.58} R^{1.08} P_{\text{net}}^{0.42} (\bar{n}_{19})^{-0.08} \times B_t^{0.06} \kappa_a^{1.81} A^{2.13} M^{0.2} F_q^{2.09}, \quad (15)$$

where  $p_{\text{ped}}^{\text{scl}}$  is the pressure of the pedestal top in Pa,  $W_{\text{ped}}^{\text{scl}}$  is the stored energy in the pedestal in MJ,  $V_p$  is the plasma volume in  $\text{m}^3$ , 0.92 denotes the fraction of the volume inside the pedestal top to  $V_p$ ,  $I_p$  is plasma current in MA,  $R$  is the plasma major radius in m,  $\bar{n}_{19}$  is the line-average electron density in  $10^{19} \text{ m}^{-3}$ ,  $\kappa_a$  is ellipticity, and  $A$  is the aspect ratio,  $F_q = q_{95}/q_{\text{cyl}}$ , and  $q_{\text{cyl}} = 5\kappa_a a^2 B_t / (RI_p)$ .

In order to match the pedestal pressure with the scaling law, pedestal pressure control is performed by the following three models: (a) the proportional-integral-differential (PID) control model, (b) the ELM model, and (c) the empirical continuous ELM model.

In (a) the PID control model, the pedestal pressure is PID controlled by using the enhancement factor of thermal diffusivity so that the pedestal pressure  $p_{\text{ped}}$  would follow the value predicted by the scaling  $p_{\text{ped}}^{\text{scl}}$ :

$$C_e^{\text{new}} = C_e + \Delta C \Delta t, \quad (16)$$

$$C_i^{\text{new}} = C_i + \frac{\Delta C}{2} \Delta t, \quad (17)$$

$$\Delta C = G_P \varepsilon + G_I \int_0^t \varepsilon dt, \quad (18)$$

$$\varepsilon = p_{\text{ped}}^{\text{scl}} - p_{\text{ped}}, \quad (19)$$

where  $G_P$  is the proportional gain,  $G_I$  is the integral gain, and  $\varepsilon$  is the pressure deviation. The  $\Delta C$  is multiplied by the time step  $\Delta t$  to prevent control from relying on the calculation time step.

The proportional gain  $G_P$  is determined from the relationship between the pedestal pressure  $p_{\text{ped}}$  and the enhancement factors  $C_e$  and  $C_i$ . Dependence on  $C_e$  of the pedestal pressure was obtained by changing  $C_e$  from 0.3 to 0.03 linearly during 50 s while keeping the ratio of  $C_e$  to  $C_i$  at 2:1. The alpha heating power was maintained at 217 MW by feedback control using the pellet injection frequency as the actuator under the external RF heating power of 200 MW. The result shown in Fig. 3 is fitted by  $p_{\text{ped}} = p_0 C_e^{-0.65}$  quite well. From this relationship, we have

$$\frac{dp_{\text{ped}}}{dC_e} = -0.65 p_0 C_e^{-1.65}, \quad (20)$$

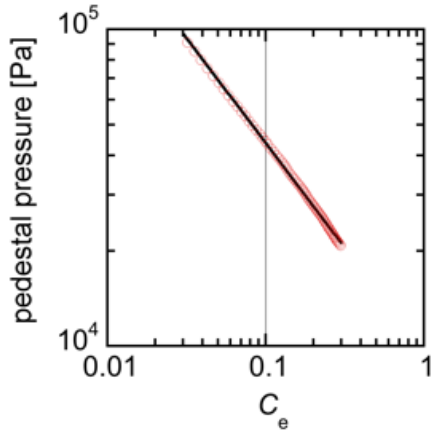


Fig. 3 Relationship of pedestal pressure  $p_{\text{ped}}$  to enhancement factor  $C_e$ . The data points (red open circles) are fitted by a function (black solid line)  $p_{\text{ped}} = 9528.7 \times C_e^{-0.66167}$ . Only one symbol is plotted per 30 data points to avoid excessive overlapping.

$$G_P = \frac{C_e^{\text{new}} - C_e}{p_{\text{ped}}^{\text{scl}} - p_{\text{ped}}} = \frac{\Delta C_e}{\Delta p} = -\frac{C_e^{1.65}}{0.65 p_0} = -\frac{C_e}{0.65 p_{\text{ped}}} (\text{Pa}^{-1}). \quad (21)$$

In the simulation the value of  $G_P$  was reduced to one third of this to avoid the back transition after the H-mode transition. The integrated gain  $G_I$  was set to  $-3 \times 10^{-8} \text{ Pa}^{-1} \text{ s}^{-1}$  in order to reduce the offset.

In (b) the ELM model, when the pedestal pressure exceeds  $p_{\text{ped}}^{\text{scl}}$ , the thermal diffusivity is increased for a short pre-determined time, and then is returned to the values in H mode. This simulates the ELM, where heat and particles are released due to instability when the pressure exceeds the pressure stability limit. An example of the results is shown in Fig. 4. When the pedestal pressure  $p_{\text{ped}}$  exceeds  $p_{\text{ped}}^{\text{scl}}$ , the enhancement factors are increased to  $C_e = 2$ ,  $C_i = 1$  during 0.2 ms. This condition was determined to have the released plasma energy  $\Delta W$  at each ELM of about 7% of the pedestal energy  $W_{\text{ped}}$  in the simulations shown in Sec. 4. In this condition, the maximum thermal diffusivity of  $\sim 100 \text{ m}^2 \text{ s}^{-1}$  is obtained as shown in Fig. 4; this value is used in the simulation in Ref. [11]. The drop of the pedestal pressure is about 60% in this case and the ELM cycle is about 250 ms. Small time steps are used to simulate release of heat and particle in a short duration of 0.2 ms. The ELM cycle depends on the drop of the pedestal pressure; smaller ELMs have shorter period. After release, the enhancement factors are returned to the values in the H-mode;  $C_e = 0.007$  and  $C_i = 0.0035$ , and then the pedestal pressure recovers. Since  $p_{\text{ped}}^{\text{scl}}$  changes significantly during each ELM cycle, mainly due to change in  $P_{\text{net}}$ , the low-pass filter described in Sec. 2.4 is applied to  $p_{\text{ped}}^{\text{scl}}$  to suppress transient change in  $p_{\text{ped}}^{\text{scl}}$ .

In (c) the empirical continuous ELM model, extra thermal diffusivity is added in the pedestal region when

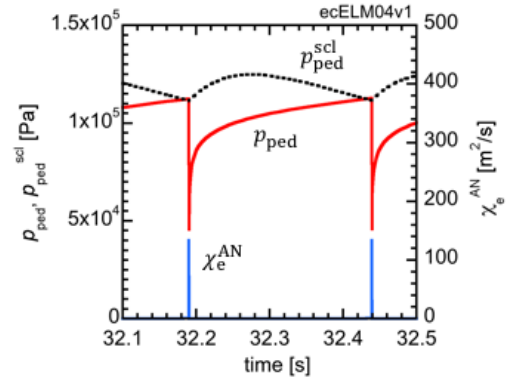


Fig. 4 Time evolution of pedestal pressure  $p_{\text{ped}}$  (red solid line), that predicted by the scaling law  $p_{\text{ped}}^{\text{scl}}$  (black dotted line) and anomalous electron thermal diffusivity  $\chi_e^{\text{AN}}$  at the pedestal top (blue solid line) in a simulation with the ELM model.

the pedestal pressure exceeds  $p_{\text{ped}}^{\text{scl}}$ . The following diffusion coefficient is added according to the pressure.

$$\chi_{\text{elm}} = \chi_0 \times \max\left(0, \frac{p_{\text{ped}}}{p_{\text{ped}}^{\text{scl}}} - 1\right)^\beta, \quad (22)$$

$$\chi_0 = 100 \text{ m}^2 \text{ s}^{-1}, \quad (23)$$

$$\beta = 1.5. \quad (24)$$

This model is based on the model used in Ref. [12], where the normalized pressure gradient to its critical value determined by the stability limit was used in place of  $p_{\text{ped}}/p_{\text{ped}}^{\text{scl}}$  with  $\chi_0 = 100 \text{ m}^2 \text{ s}^{-1}$  and  $\beta = 2$ . In this work, the value of  $\beta$  was modified to 1.5 so that  $p_{\text{ped}}$  is controlled close to  $p_{\text{ped}}^{\text{scl}}$  in the simulation. Increase in the particle diffusivity is determined by Eq. (9) when the pedestal pressure exceeds  $p_{\text{ped}}^{\text{scl}}$  and the thermal diffusivity is increased, while increase in the particle diffusivity was the same as that in the thermal diffusivity in Ref. [12].

An example of the results is shown in Fig. 5. The thermal and particle diffusivities,  $\chi_e^{\text{AN}}$ ,  $\chi_i^{\text{AN}}$  and  $D^{\text{AN}}$  are increased when  $p_{\text{ped}}$  exceeds  $p_{\text{ped}}^{\text{scl}}$  while they are decreased when  $p_{\text{ped}}$  becomes lower than  $p_{\text{ped}}^{\text{scl}}$ . The response of thermal and particle diffusivities is delayed typically by one time step. This is because the newly calculated diffusivities are not used directly but those with reduced change from the values at the previous time step, which are shown in Fig. 5, are used in the particle and heat transport equations in TOTAL in order to avoid rapid change in the diffusivity. In contrast, the  $p_{\text{ped}}$  responds to change in diffusivities without delay. As a result, the  $p_{\text{ped}}$  is kept around  $p_{\text{ped}}^{\text{scl}}$ , where the amplitude of the deviation from  $p_{\text{ped}}^{\text{scl}}$  is about 2%. The low-pass filter is applied to  $p_{\text{ped}}^{\text{scl}}$  to suppress transient change in  $p_{\text{ped}}^{\text{scl}}$ .

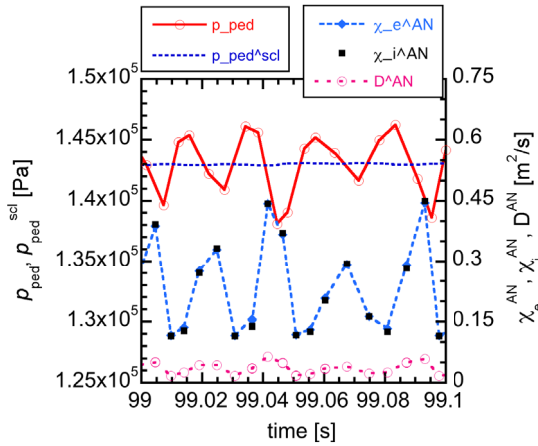


Fig. 5 Time evolution of pedestal pressure  $p_{\text{ped}}$  (red solid line), that predicted by the scaling law  $p_{\text{ped}}^{\text{scl}}$  (dark blue dotted line) and anomalous electron thermal diffusivity  $\chi_e^{\text{AN}}$  (blue dotted line), anomalous ion thermal diffusivity  $\chi_i^{\text{AN}}$  (black squares) and anomalous particle diffusivity  $D^{\text{AN}}$  (red dotted line) at the pedestal top in a simulation with the ELM model.

## 2.4 Low-pass filter

A low-pass filter is used for the purpose of suppressing oscillation in  $P_{\text{net}}$  and  $p_{\text{ped}}^{\text{scl}}$  due to changes in calculation steps in the ELM model and the empirical ELM model. It is also used to show calculation results on the pedestal pressure and the pellet injection frequency with the ELM model and the empirical continuous ELM model eliminating fluctuating components.

A low-pass filter is a type of filter that attenuates components with frequencies higher than the cutoff frequency. Since a simple low-pass filter is realized by an RC circuit consisting of a capacitor and a resistor, it is also called an RC filter. Let  $t$  be the time,  $y$  be the input voltage, and  $Y$  be the output voltage. From the RC circuit equation we have

$$Y_i + \tau \frac{Y_i - Y_{i-1}}{\Delta t_i} = y_i, \quad (25)$$

where  $i$  denotes the number in the time step,  $\Delta t_i = t_i - t_{i-1}$ , and  $\tau$  is the value of RC or the time constant. By solving the above equation for  $Y_i$  we have

$$Y_i = \frac{\tau}{\tau + \Delta t_i} Y_{i-1} + \frac{\Delta t_i}{\tau + \Delta t_i} y_i. \quad (26)$$

When it is applied to  $P_{\text{net}}$  and  $p_{\text{ped}}^{\text{scl}}$ ,  $\tau = 0.1$  s is used considering typical ELM periods.

## 3. Plasma Parameters and Conditions

In this work, Japan's DEMO (JA DEMO) design values [13] shown in Table 1 are used. The boundary conditions of the electron density and the ion/electron temperature are  $2 \times 10^{19} \text{ m}^{-3}$ , 740 eV and 350 eV, respectively, at the edge. These values were taken from those used in study on power exhaust and divertor design in JA

Table 1 Parameter of JA DEMO.

parameter		value
Plasma major radius	$R_p(\text{m})$	8.5
Plasma minor radius	$a_p(\text{m})$	2.42
Aspect ratio	$A$	3.5
Elongation	$\kappa_{95}$	1.65
Triangularity	$\delta_{95}$	0.33
Safety factor	$q_{95}$	4.1
Plasma volume	$V_p(\text{m}^3)$	1647
Plasma current	$I_p(\text{MA})$	12.3
Toroidal magnetic field	$B_T(\text{T})$	5.94

DEMO [14]. The initial electron density is given so that it is  $4.64 \times 10^{19} \text{ m}^{-3}$  at the center and is  $4 \times 10^{19} \text{ m}^{-3}$  in line average. This value was determined considering the shine-through of neutral beam (NB) though lower density would be preferable for reducing heating power for H mode access. A similar density before high power NB heating was also assumed in a study on operation scenario in ITER [15]. The initial temperature is 3 keV in the center. The DT ratio of plasma and pellet is 1:1. The density of helium was 5% of the electron density. No impurities other than helium are considered, except for simulations shown in Sec. 5.

In JA DEMO, NB heating and electron cyclotron (EC) wave heating will be employed [13]. A Fokker-Planck solver for analysis of heating and current drive with NB injection has been installed in TOTAL [16] while no modules for EC wave analysis are available. In this work, for simplicity, we do not use the Fokker-Planck solver but give heating power, without particle fueling, in a fixed radial profile. We call this RF heating. Its power is 10 MW before  $t = 10$  s, is increased to 120 MW at  $t = 10$  s, is decreased to 83.5 MW at  $t = 15$  s, and is kept constant after that; the waveform is shown in Fig. 6 (b). The fractions of ion heating power and electron heating power are 0.25 and 0.75, respectively.

The line-average electron density is PID controlled by using pellet injection rate [2]. The proportional, integral and differential gains for the density control is  $G_P^{\text{pellet}} = 3000$ ,  $G_I^{\text{pellet}} = 5 \text{ s}^{-1}$  and  $G_D^{\text{pellet}} = 3000 \text{ s}$ , respectively. Cylindrical pellets with diameter of 4 mm and height of 4 mm are assumed to be injected from the high magnetic field side with velocity of 0.3 km/s. The target value of the line-average electron density is increased linearly from  $4 \times 10^{19} \text{ m}^{-3}$  at  $t = 0$  s to  $8.5 \times 10^{19} \text{ m}^{-3}$  at  $t = 80$  s and then is kept constant; the waveform is shown in Fig. 6 (a).

The value of flat-top heating power (83.5 MW) is that assumed in pulse operation of JA DEMO [13] where alpha heating power of 217 MW or fusion power of 1.09 GW is planned, while the line-average electron density ( $8.5 \times 10^{19} \text{ m}^{-3}$ ) is close to that assumed in pulse operation of JA DEMO [13]. The size and velocity of pellets are similar to

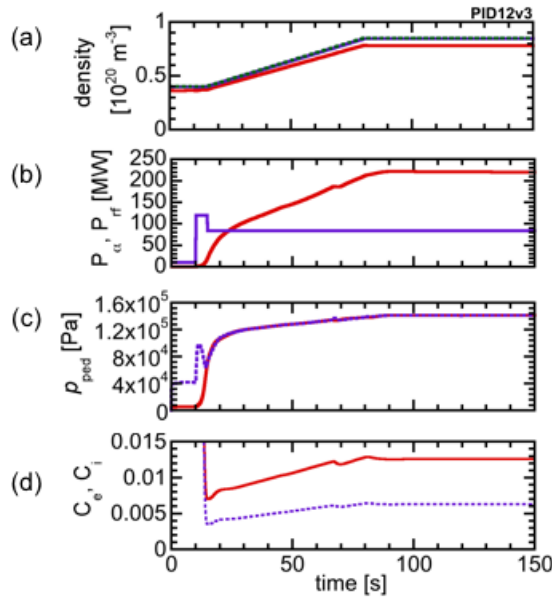


Fig. 6 Results of simulation with the PID control model. (a) The line-average electron density (blue), its target value (green, dotted) and the volume-average electron density (red). The first two are nearly identical and overlapped. (b) The alpha heating power (red) and the RF heating power (purple). (c) The pedestal pressure  $p_{\text{ped}}$  (red) and that predicted by the scaling law  $p_{\text{ped}}^{\text{sc1}}$  (purple, dotted). (d) The enhancement factors  $C_e$  (red) and  $C_i$  (purple, dotted).

those planned for ITER [17].

## 4. Comparison of Pedestal Pressure Control Models

The simulation from L-mode plasma with low heating power to H-mode plasma with high fusion power is performed using the three pedestal pressure control models, with the same external heating power and the same target density as described in the previous section. The calculation is identical to that shown in Fig. 2 for three models until the end of L to H transition phase,  $t = 15.6$  s. The pedestal pressure control is started with three different models from that time, when the pedestal pressure reaches  $p_{\text{ped}}^{\text{sc1}}$ .

### 4.1 PID control model

Figure 6 shows the results of the simulation with the PID control model. The line-average density follows the target value and reaches  $8.5 \times 10^{19} \text{ m}^{-3}$  at  $t = 80$  s as shown in Fig. 6 (a). The alpha power reaches 220 MW, which is close to the design value, at  $t = 150$  s as shown in Fig. 6 (b). Time evolution of  $p_{\text{ped}}$  and  $p_{\text{ped}}^{\text{sc1}}$  is shown in Fig. 6 (c). The pedestal pressure  $p_{\text{ped}}$  is controlled exactly to the pressure limit  $p_{\text{ped}}^{\text{sc1}}$  until the end of simulation,  $t = 150$  s. The increase in  $p_{\text{ped}}^{\text{sc1}}$  is due to increase in  $P_{\text{net}}$ . Since dependence of  $p_{\text{ped}}^{\text{sc1}}$  on  $P_{\text{net}}$  is  $P_{\text{net}}^{0.42}$ , from Eqs. (14) and (15), the  $C_e$

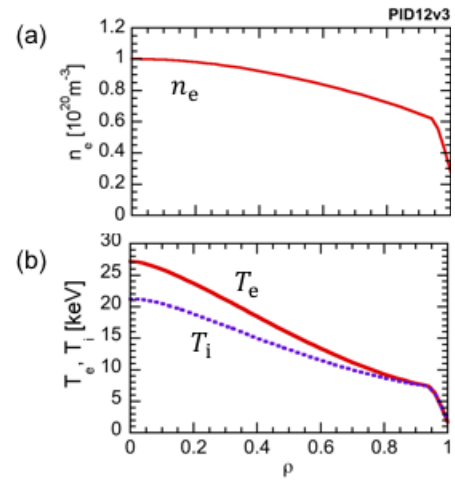


Fig. 7 Radial profiles of (a) the electron density  $n_e$ , (b) the electron temperature  $T_e$  (red, solid) and the ion temperature  $T_i$  (purple, dotted) at  $t = 150$  s of the simulation shown in Fig. 6.

and  $C_i$  need to be increased to keep relation  $p_{\text{ped}} = p_{\text{ped}}^{\text{sc1}}$ . Such adjustment is properly performed with this model as shown in Fig. 6 (d). The radial profiles of the electron density  $n_e$ , the electron temperature  $T_e$  and the ion temperature  $T_i$  at  $t = 150$  s are shown in Fig. 7. At the pedestal top,  $n_e = 6.2 \times 10^{19} \text{ m}^{-3}$ ,  $T_e = T_i = 7$  keV. The  $n_e$  profile is moderately peaked due to inward particle pinch while the fueling with pellet injection is located around  $\rho = 0.8$ , where  $\rho$  is the normalized minor radius.

### 4.2 ELM model

Figure 8 shows the results of the simulation with the ELM model. The line-average density is lower than the target value as shown in Fig. 8 (a) though fueling was larger than in the PID model as shown in Fig. 8 (d); the pellet injection frequency is about 5 Hz after  $t = 80$  s in the ELM model case while it is about 0.5 Hz in the PID model case. The alpha power reaches 300 MW as shown in Fig. 8 (b) in spite of lower line-average electron density. The time evolution of  $p_{\text{ped}}$  and  $p_{\text{ped}}^{\text{sc1}}$  is shown in Fig. 8 (c). The pedestal pressure is controlled lower than  $p_{\text{ped}}^{\text{sc1}}$  with repetitive ELMs.

The radial profiles of  $n_e$  and  $T_i$  at  $t = 150$  s are shown in Fig. 9. The pedestal density is significantly lower than in the PID model case shown by blue dotted line. The pedestal temperature is instead higher in the ELM model case. The density is similar and the temperature is higher in the central region in the ELM model case, which leads to higher fusion power. It is interesting that lower pedestal density is observed in the ELM model case though relation between the particle diffusivity and the thermal diffusivity is not changed, given by Eq. (9) in both of PID model and ELM model cases. One possible cause is difference in the location of particle source and the heat source, the former

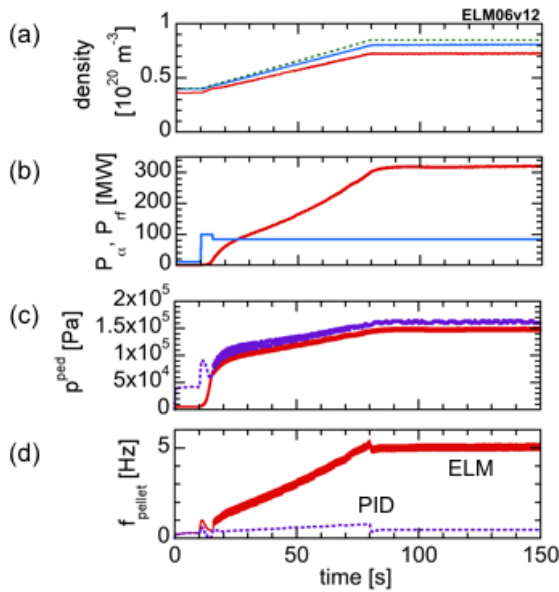


Fig. 8 Results of simulation with the ELM model. (a) The line-average electron density (blue), its target value (green) and the volume-average electron density (red). (b) The alpha heating power (red) and the RF heating power (blue). (c) The pedestal pressure  $p_{\text{ped}}$  (red) and that predicted by the scaling law  $p_{\text{ped}}^{\text{sc1}}$  (purple, dotted). (d) The pellet injection frequency with that in the simulation with the PID model shown in Fig. 6 (purple, dotted). The low pass filter is applied to  $p_{\text{ped}}$ ,  $p_{\text{ped}}^{\text{sc1}}$ , and the pellet injection frequency.

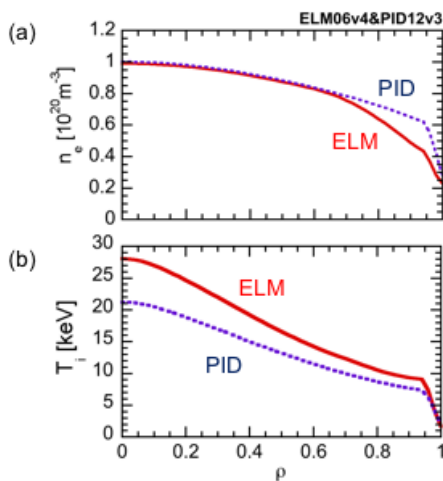


Fig. 9 Radial profiles of (a) the electron density  $n_e$  and (b) the ion temperature  $T_i$  at  $t = 150$  s of the simulation with the ELM model shown in Fig. 8 (red, solid) compared with that with the PID model shown in Fig. 6 (purple, dotted).

is closer to the edge.

### 4.3 Empirical continuous ELM model

Figure 10 shows the results of the simulation with the empirical continuous ELM model. All of the elec-

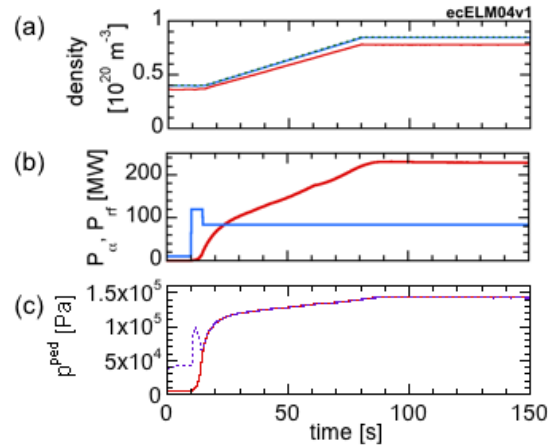


Fig. 10 Results of simulation with the empirical continuous ELM model. (a) The line-average electron density (blue), its target value (green) and the volume-average electron density (red). The first two are nearly identical and overlapped. (b) The alpha heating power (red) and the RF heating power (blue). (c) The pedestal pressure  $p_{\text{ped}}$  (red) and that predicted by the scaling law  $p_{\text{ped}}^{\text{sc1}}$  (purple, dotted). The low pass filter is applied to  $p_{\text{ped}}$  and  $p_{\text{ped}}^{\text{sc1}}$ .

tron density, alpha heating power and the pedestal pressure are close to those in the PID control model shown in Fig. 6, though we have fluctuations in the pedestal pressure as shown in Fig. 5, which are eliminated owing to the low pass filter in Fig. 10. The  $p_{\text{ped}}$  is controlled close to  $p_{\text{ped}}^{\text{sc1}}$ . The pellet injection frequency, not shown, is nearly identical to that in the PID control model.

### 4.4 Summary of comparison of three models

Nearly the same results are obtained with the PID control model and with the empirical continuous ELM model, while different results are obtained with the ELM model. The computational cost is the lowest in the PID control model and the highest in the ELM model.

Higher pellet-injection frequency, namely a larger amount of fueling, is needed in the ELM model to raise the density close to the target value than in the PID control model and in the empirical continuous ELM model. These differences suggest that modeling of ELM including its frequency and the amount of release of particles is important to predict required amount of fueling and the density profile. However, the simulation in this study employs fixed edge values for the density and the temperature. It would not be the case in experiment. It would be needed to include the transport in the SOL plasma to evaluate the boundary values of the density and then evaluate the required fueling precisely.

## 5. Simulation on Impurity Injection

Response to tungsten impurity injection is simulated and compared with the PID control model and the empir-

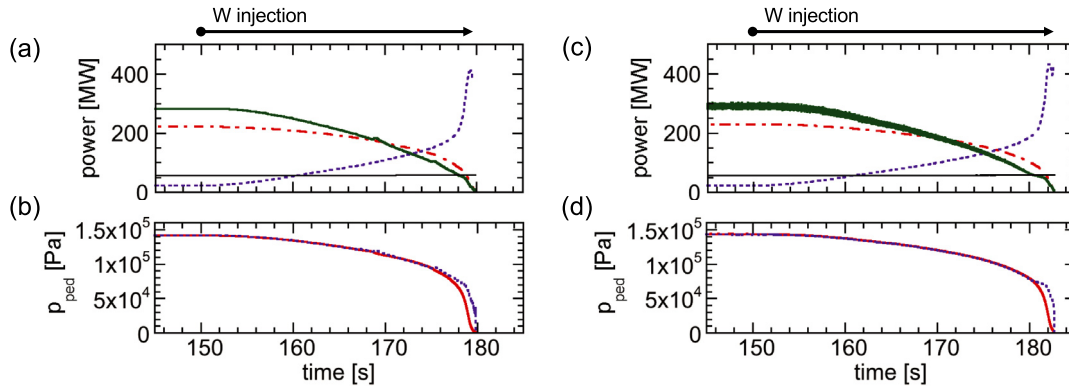


Fig. 11 Simulation on impurity injection with (left) the PID model and (right) the empirical continuous ELM model. Time evolution of (a), (c) the alpha heating power (red chain-dashed), radiation power (purple, dotted), net power  $P_{\text{net}}$  (green), and  $P_{\text{HL}}$  (black). (b), (d)  $p_{\text{ped}}$  (red) and  $p_{\text{ped}}^{\text{scl}}$  (purple).

ical continuous ELM model. The heating power is sustained at 83.5 MW. The target value of the line-average electron density is  $8.5 \times 10^{19} \text{ m}^{-3}$ . Tungsten atoms are injected on the plasma surface with energy of 10 eV. Injection is started at  $t = 150$  s. The injection rate per unit plasma surface is linearly increased to  $2 \times 10^{17} \text{ m}^{-2} \text{ s}^{-1}$  at  $t = 160$  s and is kept constant. The final values correspond to 51 mg/s of injected mass of tungsten.

The results are shown in Fig. 11. The behavior is quite similar in both cases. The  $p_{\text{ped}}^{\text{scl}}$  decreases after tungsten injection because of decreased net power due to increased radiation. The H to L transition takes place around  $t = 180$  s when  $P_{\text{net}}$  reaches  $P_{\text{HL}}$ . After that the radiation power rises quickly, the  $P_{\text{net}}$  becomes nearly zero and then the calculation is terminated. The pedestal pressure control is terminated at the H to L transition. In the PID control model,  $p_{\text{ped}}$  starts to deviate from  $p_{\text{ped}}^{\text{scl}}$  around  $t = 177$  s, slightly before the H to L transition, while in the empirical continuous ELM model,  $p_{\text{ped}}$  follows  $p_{\text{ped}}^{\text{scl}}$  until the end of the H-mode phase.

## 6. Summary

An algorithm to trigger the transition between the L mode and the H-mode and three types of models for controlling the pedestal pressure in the H-mode were introduced into the TOTAL code. The models were tested on Japan's DEMO plasma. At the L to H transition, quick reduction in transport in the pedestal region causes back transition due to reduced net heating power and therefore gradual change in the transport in the pedestal region is needed. In the PID control model, the pedestal pressure is adjusted accurately to the target value. In the ELM model, the pressure drops significantly during each ELM and it requires large pellet injection to increase the density. In the empirical continuous ELM model, the pedestal pressure is adjusted as in the PID control model, though some fluctuations are generated in the pedestal pressure. Radial profiles

of the electron density and the ion temperature are different in the ELM model compared to the other two models. Response to tungsten impurity injection into H-mode plasma was simulated with the PID control model and the empirical continuous ELM model. The pedestal pressure predicted by the scaling law decreases through reduction of net heating power due to enhanced radiation power, until the transition to the L-mode takes place. The pedestal pressure follows the target value in both models, though slight deviation is observed just before the H to L transition in the PID control model.

The required particle fueling rate and the density/temperature profiles depends on the pedestal pressure control models even though the same formula is employed for the prediction on the pedestal pressure. It would be needed to include the SOL transport models and also to compare the calculation with the experiment, as future work.

## Acknowledgments

This work was carried out as a part of the tokamak plasma collaboration research program in National Institutes for Quantum and Radiological Science and Technology and of the collaboration research programme of Joint Special Design Team for fusion DEMO in Japan.

- [1] C.E. Kessel *et al.*, Nucl. Fusion **55**, 063038 (2015).
- [2] R. Sakai *et al.*, Plasma Fusion Res. **15**, 1303031 (2020).
- [3] T.J.J. Tara *et al.*, Plasma Phys. Control. Fusion **43**, 507 (2001).
- [4] A. Taroni *et al.*, Plasma Phys. Control. Fusion **36**, 1629 (1994).
- [5] M. Erba *et al.*, Plasma Phys. Control. Fusion **39**, 261 (1997).
- [6] Y. Shimizu *et al.*, Plasma Fusion Res. **10**, 3403062 (2015).
- [7] W.A. Houlberg *et al.*, Phys. Plasmas **4**, 3230 (1997).
- [8] Y.R. Martin *et al.*, J. Physics: Conf. Ser. **123**, 012033 (2008).
- [9] F. Ryter *et al.*, J. Phys. Conf. Ser. **123**, 012035 (2008).
- [10] J.G. Cordey *et al.*, Nucl. Fusion **43**, 670 (2003).

- [11] N. Hayashi *et al.*, Nucl. Fusion **47**, 682 (2007).  
[12] V. Parail *et al.*, Nucl. Fusion **49**, 075030 (2009).  
[13] Y. Sakamoto *et al.*, 27th IAEA Fusion Energy Conf. (Ahmedabad) IAEA-CN-258 FIP/3-2 (2018).  
[14] N. Asakura *et al.*, Nucl. Fusion **57**, 126050 (2017).  
[15] S.H. Kim *et al.*, Nucl. Fusion **58**, 056013 (2018).  
[16] R. Funabashi *et al.*, Plasma Fusion Res. **15**, 2401071 (2020).  
[17] A.R. Polevoi *et al.*, Nucl. Fusion **57**, 022014 (2017).